PROCEEDINGS A

royalsocietypublishing.org/journal/rspa

Research



Cite this article: Thomson SJ, Durey M, Rosales RR. 2020 Collective vibrations of a hydrodynamic active lattice. *Proc. R. Soc. A* **476**: 20200155.

http://dx.doi.org/10.1098/rspa.2020.0155

Received: 5 March 2020 Accepted: 5 June 2020

Subject Areas:

applied mathematics, fluid mechanics

Keywords:

active particles, amplitude equations, bifurcations, collective behaviour, coupled oscillators

Author for correspondence:

S. J. Thomson

e-mail: thomsons@mit.edu

Electronic supplementary material is available online at https://doi.org/10.6084/m9.figshare. c.5056722.

THE ROYAL SOCIETY PUBLISHING

Collective vibrations of a hydrodynamic active lattice

S. J. Thomson, M. Durey and R. R. Rosales

Department of Mathematics, Massachusetts Institute of Technology, Cambridge, MA 02139, USA

SJT, 0000-0003-1101-6457; MD, 0000-0002-4232-1705

Recent experiments show that quasi-one-dimensional lattices of self-propelled droplets exhibit collective instabilities in the form of out-of-phase oscillations and solitary-like waves. This hydrodynamic lattice is driven by the external forcing of a vertically vibrating fluid bath, which invokes a field of subcritical Faraday waves on the bath surface, mediating the spatio-temporal droplet coupling. By modelling the droplet lattice as a memory-endowed system with spatially non-local coupling, we herein rationalize the form and onset of instability in this new class of dynamical oscillator. We identify the memorydriven instability of the lattice as a function of the number of droplets, and determine equispaced lattice configurations precluded by geometrical constraints. Each memory-driven instability is then classified as either a super- or subcritical Hopf bifurcation via a systematic weakly nonlinear analysis, rationalizing experimental observations. We further discover a previously unreported symmetry-breaking instability, manifest as an oscillatory-rotary motion of the lattice. Numerical simulations support our findings and prompt further investigations of this nonlinear dynamical system.

1. Introduction

Classifying emergent properties of many-body systems, both passive and active, is a central theme of contemporary soft matter physics [1,2]. In recent years, myriad systems have emerged whose complex dynamics at the macroscale originate from the properties of their constituent particles, such as the particles' shape, polarity, and activity or locomotion. Examples include the complex flows arising from active stresses exerted by bacteria suspended in fluid [3,4]; vortex generation and nonlinear wave propagation in colloidal fluids [5–8]; phonon-like excitations in passively driven crystals of

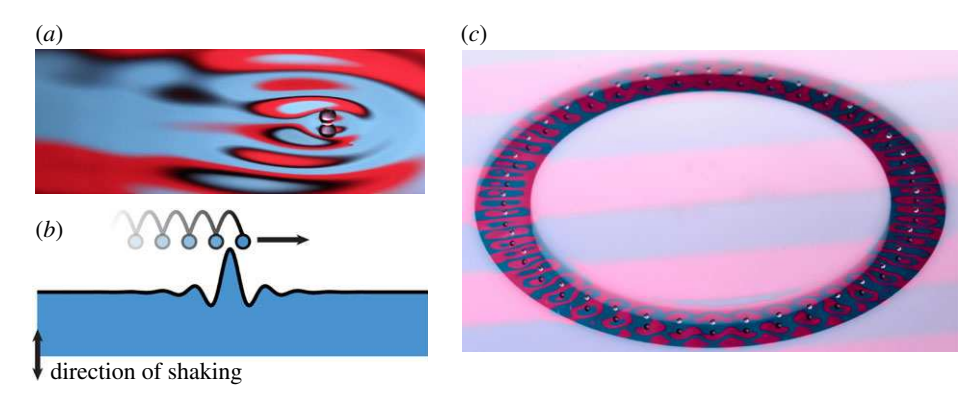


Figure 1. (a) Single droplet of silicone oil self-propelling on the surface of a vibrating fluid bath. Picture courtesy of Daniel Harris. (b) Schematic of the droplet self-propulsion. Each time the droplet impacts the bath, it experiences a lateral force from the slope of the waves excited on the surface at previous impacts. (c) Oblique perspective of a chain of 40 equispaced bouncing droplets of silicone oil confined to a submerged annular channel, surrounded by a shallow layer of fluid [25]. (Online version in colour.)

particles and droplets confined to microfluidic channels [9–13]; and emergent magnetic order in hydrodynamic spin lattices of walking dropets [14,15]. In non-fluidic systems, theoretical models of active nonlinear lattices are shown to exhibit instabilities in the form of out-of-phase oscillations and solitary waves [16–20], prompting experimental analogues in the form of active electronic circuits [21–24].

Inspired by recent experiments [25], we here focus on rationalizing the instability of a new class of fluid-based, active oscillator; see figure 1c. The active units in the experiments [25] are selfpropelled millimetric droplets bouncing on the surface of a vertically vibrating bath of viscous fluid, as described in [26,27] and references therein. In the absence of drops, the fluid interface remains flat below the Faraday threshold, the critical vibrational acceleration at which Faraday waves spontaneously appear on the bath surface. When placed on the surface, a millimetric droplet may bounce periodically in resonance with its self-generated, subcritical, subharmonic Faraday wave field (with a characteristic wavelength λ_F), exciting waves at each impact. Above a critical vibrational acceleration, the droplet destabilizes to small, lateral perturbations. In this regime, dissipative effects due to drag are overcome by propulsive forces enacted by the slope of the droplet's guiding wave field, its so-called pilot wave (figure 1a,b). Herein lies the active component of the droplet motion: self-propulsion is achieved by continual exchange of energy of the droplet with its environment, in this case the vertically vibrating fluid bath. In prevailing model systems of active matter, such as bacterial or colloidal suspensions, the dynamics of the constituent particles and their environment are typically overdamped [28,29]. This constrasts with the droplet system, wherein inertial effects play a significant role through both the finite mass of the droplets and the underdamped Faraday waves excited on each impact with the bath. Moreover, as the bath's vibrational acceleration is increased progressively, the decay time T_M of the pilot wave lengthens and the droplet is thus influenced by more of its past, increasing the socalled memory time of the droplet's motion [30]. Memory and self-propulsion are thus intimately connected, the former regulating the strength of the propulsive wave force required to overcome dissipation.

As demonstrated in [25], when confined to a submerged annular channel, droplets may form an effectively one-dimensional lattice (figure 1c). Each droplet in the lattice bounces in periodic synchrony with period T_F , generating a spatially non-local, quasi-monochromatic wave field, whose superposition over all the droplets mediates the spatio-temporal coupling of the lattice. For sufficiently large forcing, experiments show that the droplet lattice exhibits collective vibrations in the form of small-amplitude out-of-phase oscillations or solitary-like waves, depending on the

proximity of neighbouring droplets. Moreover, the transition to each of the aforementioned states may be characterized by the onset of a super- and subcritical Hopf bifurcation, respectively.

Oscillations of the lattice emerge from the competition between droplet self-propulsion—arising through the interaction of each droplet with the slope of its own wave field—and wave-mediated coupling between droplets. This latter phenomenon represents a distinguishing feature of this new class of coupled oscillator: the waves produced at each droplet impact with the bath giving rise to an effective self-generated, dynamic coupling potential between droplets (*visà-vis* lattices subject to an externally applied potential). The existence of this dynamic potential has far-reaching consequences; for example (i) there exist stable lattice equilibria in which the droplets sit at the *local maxima* of the potential and (ii) the dynamic potential encodes the memory of the system, storing information regarding each droplet's past trajectory. We note that while oscillators containing spatial and temporal non-locality have received significant theoretical attention [31–34], experimental, mechanical analogues are relatively scarce, limited to networks of coupled pendula [35,36].

Through a systematic analysis of the simplest possible model of the hydrodynamic lattice introduced in §2—we herein seek to delineate the conditions under which qualitatively different bifurcations can arise, elucidating the key mechanims underpinning the emergent, collective properties of this new class of dynamical oscillator. In §3, we identify the memory-driven, oscillatory instability of the lattice, as well as equispaced configurations rendered uniformly unstable at all memory by the form of the lattice wave field. We rationalize the latter in the low-memory regime through an energy-like quantity that the system attempts to minimize. A weakly nonlinear analysis (§4) then prescribes to each memory-driven instability a super- or subcritical Hopf bifurcation, rationalizing experimental observations [25]. Furthermore, we show that symmetry-breaking leads to a previously unreported self-induced, oscillatory-rotary motion of the lattice. Our analysis concludes in §5 with an exploration into how the transition to each of the aforementioned instabilities is controlled by the droplet separation distance. We note that, while our study is focused on the regime where droplet motion is confined to an annular channel, the results of §§2-5 are also appropriate for describing azimuthal oscillations of droplet rings in free space [37], allowing us to rationalize behaviour in this related system. Finally, the results of our paper are summarized in §6, along with proposals for future work.

2. Active lattice model

We begin by constructing a model of the droplet lattice, valid below and near to the onset of instability, following the framework set forth for a single droplet in [38]. Consider a lattice of N droplets of equal mass m, bouncing periodically with period T_F , in synchrony with the surface of the vibrating fluid bath. On successive impacts with the bath, each droplet excites a field of standing waves, the superposition of which creates a global wave field, a dynamic potential, mediating the spatio-temporal coupling of the lattice. (We ignore the effect of the initial transient wave propagating away from the impact site [27,39], as this effect is only significant when droplets are packed closely together.) Denoting by $x_n(t)$ the position of each droplet in the lattice at time t, time-averaging the droplets' horizontal motion over one bouncing period gives rise to the stroboscopic equation of motion [38]

$$m\ddot{x}_n + D\dot{x}_n = -mg\nabla \bar{h}(x,t)|_{x=x_n},$$
(2.1a)

where $\bar{h}(x,t)$ is the stroboscopic global wave field and dots denote differentiation with respect to time. According to (2.1*a*), the trajectory of each droplet is therefore governed by a balance between inertia, a time-averaged drag force with drag coefficient D [40], and the time-averaged horizontal propulsive wave force enacted on each droplet by the slope of the global wave field, $\bar{h}(x,t)$. The remaining constant g is acceleration due to gravity.

In the physical regimes of interest [25], the time scale of the droplets' vertical motion, T_F , is typically much less than the time scale of horizontal motion. The time-averaged stroboscopic wave kernel $\overline{\mathcal{H}}$ generated over each bouncing period by each droplet is thus assumed to be

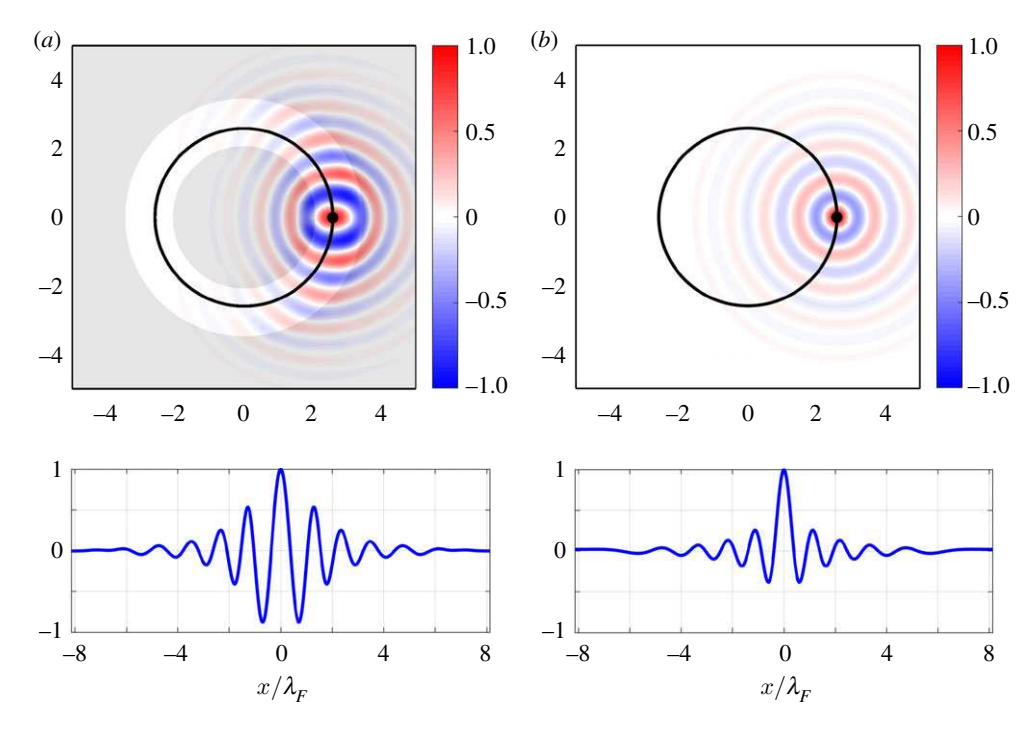


Figure 2. (a) An example wave field $\overline{\mathcal{H}}(x;x_p)$, corresponding to a stationary, bouncing droplet at $x=x_p$, computed using the model of Durey $et\ al.$ [44] for $R/\lambda_F=2.59$ (upper panel). The fluid and geometry parameters are listed in the electronic supplementary material. Grey regions denote the shallow layer of fluid, and the deeper, annular channel has a white background. The position x_p is denoted by the black dot. Horizontal lengths are normalized by the Faraday wavelength, λ_F , and the vertical scale is normalized by $\overline{\mathcal{H}}(x_p;x_p)$. The radial cut |x|=R (denoted by the black circle in the upper panel) of $\overline{\mathcal{H}}$ is presented in the lower panel, parametrized by the arc length, x, where x=0 corresponds to the horizontal position $x=x_p$. (b) The analogous result to (a) for the wave field $\overline{\mathcal{H}}(x;x_p)=F_0(|x-x_p|)$ defined by (2.3). (Online version in colour.)

the time-averaged wave field generated by a single, stationary droplet bouncing periodically at a horizontal position $x=x_p$, normalized by the exponential decay time, T_M , of the Faraday waves [41–43]. We recall from the discussion in §1 that T_M increases with the strength of the vibrational forcing of the bath [40,42]; hence, T_M may be regarded as a control parameter in our model and a proxy for increasing vertical vibrational acceleration. Increasing T_M results in a longer path memory of the droplets' past trajectory. In contrast to free space [38], we note that the presence of the annular subsurface topography in experiments [25] means that $\overline{\mathcal{H}}$ is not translationally invariant; the wave kernel depends on the position x_p at which the droplet resides in the channel and so $\overline{\mathcal{H}} = \overline{\mathcal{H}}(x;x_p)$. However, we note that the geometry of the experimental system is rotationally invariant; thus, in polar coordinates (whose origin coincides with the centre of the annulus) we have $\overline{\mathcal{H}} = \overline{\mathcal{H}}(r;r_p;\theta-\theta_p)$ (figure 2a).

A distinguishing feature of the pilot-wave system is that the horizontal wave force $-mg\nabla \bar{h}(x_n(t),t)$ depends explicitly on the droplets' past, through vestiges of the surface waves excited at previous impacts. As shown in [38], the stroboscopic wave field $\bar{h}(x,t)$ may be written as an integral over time, representing the superposition of waves generated along each droplet's prior trajectory. (This approximation remains valid provided the time scale of horizontal motion is much greater than T_F .) Alternatively, it is readily verified that $\bar{h}(x,t)$ satisfies the following partial differential equation:

$$\frac{\partial \overline{h}}{\partial t} + \frac{1}{T_M} \overline{h} = \frac{1}{T_F} \sum_{m=1}^{N} \overline{\mathcal{H}}(x; x_m). \tag{2.1b}$$

The rate of change of \bar{h} is thus balanced by wave dissipation and the generation of waves about the instantaneous position of each droplet. The integral form of the stroboscopic model is recovered by integrating (2.1*b*).

The system (2.1) is the many-droplet analogue of the stroboscopic model presented in [38, 45], generalized to account for submerged topography. In the experiments reported in [25], it is observed that, close to the point of instability, the deviation from circumferential droplet motion is small. Using this fact, we recast the two-dimensional horizontal droplet motion, given by (2.1), in terms of the arc length x along a circle of constant radius R (which, in experiments, is controlled by the radius of the submerged channel). The projection of the stroboscopic wave kernel, $\overline{\mathcal{H}}$, onto this circle is then $\mathcal{H}(x) = \overline{\mathcal{H}}(Re_r(x); Re_r(0))$, where the radial unit vector $e_r(x)$ is defined as $e_r(x) = (\cos(x/R), \sin(x/R))$. Furthermore, the rotational invariance of the system renders $\mathcal{H} = \mathcal{H}(x - x_p)$, where the wave kernel $\mathcal{H}(x)$ is periodic with period $L = 2\pi R$. The model (2.1) then becomes

$$m\ddot{x}_n + D\dot{x}_n = -mg\frac{\partial h}{\partial x}\Big|_{x=x_n}$$
 (2.2a)

and

$$\frac{\partial h}{\partial t} + \frac{1}{T_M} h = \frac{1}{T_F} \sum_{m=1}^{N} \mathcal{H}(x - x_m), \tag{2.2b}$$

where h(x, t) is the global wave field projected along the circle of radius R.

Our model is closed by selecting a particular form of the wave kernel $\mathcal{H}(x) = \mathcal{H}(x+L)$, which may be generated using a fluid mechanical model to compute the fluid evolution over the submerged annular channel [44] (figure 2a). However, there are many subtle aspects of the wave field that obfuscate the key mechanisms underlying the dynamics of the hydrodynamic lattice. These include variations in the wave-field amplitude arising due to the particular bouncing phase of the drops [43], and memory-dependent changes to the exponential decay length of the pilot wave [46–49]. Our theory is instead developed for a general, flexible, periodic wave kernel, $\mathcal{H}(x)$. For exploration and demonstration purposes, we simply define a wave kernel that exhibits the fundamental aspects of the fluid system: namely, a quasi-monochromatic wave field endowed with exponential spatial decay, exhibiting a peak at the droplet position. An application—using the results of this study—to the specific fluid system explored in experiments is subject to future work.

To inform our choice of candidate wave kernel, $\mathcal{H}(x)$, we observe numerically that topographically induced deviations in $\overline{\mathcal{H}}(x;x_p)$ from an axisymmetric wave kernel about x_p are weak (figure 2a). For simplicity, we thus consider $\overline{\mathcal{H}}(x;x_p) = F_0(|x-x_p|)$ for our simulations, where a candidate monochromatic, axisymmetric wave form $F_0(r)$ exhibiting exponential spatial decay is

$$F_0(r) = A_0 J_0(k_F r) \operatorname{sech}\left(\frac{r}{l_d}\right). \tag{2.3}$$

Here, J_0 is the zeroth-order Bessel function as arises for droplets in free space, modulated to incorporate spatial damping of the wave kernel [42,43,49]. The parameter A_0 is the wave amplitude, $k_F = 2\pi/\lambda_F$ is the Faraday wavenumber and l_d is a tunable spatial decay length, which in turn determines the strength of the non-local droplet coupling. The wave kernel, $\mathcal{H}(x)$, is then defined as the radial cut of $\overline{\mathcal{H}}(x;x_p)$ along a circle of constant radius R, specifically

$$\mathcal{H}(x) = F_0 \left(2R \sin \frac{x}{2R} \right), \tag{2.4}$$

as demonstrated by the black circle in figure 2b. A further advantage of (2.4) is that it allows us to easily explore the implications of varying the lattice radius, R, continuously (§5). For peace of mind, we tested this generic wave kernel against a numerically computed wave kernel [44], which demonstrated sufficient qualitative similarities to still capture the dynamical motion of the active lattice (see electronic supplementary material for further details). Finally, we emphasize that the analysis presented herein is independent of the particular choice of \mathcal{H} , provided that \mathcal{H} is periodic and sufficiently smooth.

To non-dimensionalize (2.2)–(2.4), we set λ_F as the typical horizontal length scale, $t_0 = m/D$ as the typical time scale, and $h_0 = \lambda_F^2/gt_0^2$ as the typical free-surface elevation. By rescaling $\mathcal{H} \mapsto \mathcal{H}_0\mathcal{H}$, where $\mathcal{H}_0 = h_0 T_F/t_0$, the dimensionless model then reads

$$\ddot{x}_n + \dot{x}_n = -\frac{\partial h}{\partial x}(x_n, t) \tag{2.5a}$$

and

$$\frac{\partial h}{\partial t} + \nu h = \sum_{m=1}^{N} \mathcal{H}(x - x_m), \tag{2.5b}$$

where

$$\mathcal{H}(x) = F\left(2r_0 \sin \frac{x}{2r_0}\right), \quad F(r) = \mathcal{A}J_0(2\pi r)\operatorname{sech}\left(\frac{r}{l}\right). \tag{2.6}$$

The dimensionless parameters are $l = l_d/\lambda_F$, $r_0 = R/\lambda_F$, $v = t_0/T_M > 0$, and $\mathcal{A} = \mathcal{A}_0/\mathcal{H}_0$, while the dimensionless circumference of the lattice is $\Lambda = L/\lambda_F = 2\pi r_0$. Unless stated otherwise, for the numerical results presented herein, we consider values typical of experiments, namely $r_0 = 5.4$ [25], $\mathcal{A} = 0.1$, and l = 1.6 [42].

To summarize, waves are generated about the current position of each droplet and superpose to form the global wave field, h(x,t). The spatio-temporal evolution of h(x,t) is regulated by (2.5b) and depends on the trajectories of each droplet, imprinting a path-memory on the system. Each droplet is then driven by the local gradient of h(x,t) through (2.5a). The effects of memory (and hence of vibrational acceleration) in our dimensionless system (2.5) are encoded through the dimensionless dissipation rate $\nu \sim 1/T_M$. While ν is convenient algebraically, we will interpret our results using a more natural measure of memory $M=1/\nu$, where larger M means that past dynamics play a more prominent role.

3. Memory-driven and geometric instability

To determine the critical value of the memory $M=M_c$ at which the wave force promotes self-propulsion of the droplets, we analyse the linear stability of (2.5) to small perturbations about a static, equispaced lattice configuration, coinciding with experiments [25]. Initially, the droplets are positioned at $x_n=n\delta$, where $\delta=\Lambda/N$. Equation (2.5*b*) then yields the corresponding free-surface elevation

$$h(x) = h_0(x) = \frac{1}{\nu} \sum_{m=1}^{N} \mathcal{H}(x - m\delta).$$
 (3.1)

By symmetry, the free-surface gradient beneath each droplet vanishes in this steady configuration. We note that as the wave field h is a dynamic and not a static potential, the form of $\mathcal H$ permits stable lattice configurations in which each droplet resides at a local maximum of h. Furthermore, from (3.1), we see that one effect of increasing the memory, $M = 1/\nu$, is to increase the wave amplitude of the steady lattice. Upon consideration of a small perturbation to each droplet position, x_n , and the concomitant perturbation to the wave field, h, we set

$$x_n = n\delta + \eta \hat{x}_n$$
 and $h = h_0 + \eta \hat{h}_n$

where $0 < \eta \ll 1$. By substituting this form into (2.5) and linearizing, we obtain

$$\ddot{x}_n + \dot{x}_n = -\left[\frac{\partial h}{\partial x} + x_n \frac{\partial^2 h_0}{\partial x^2}\right]\Big|_{x=n\delta}$$
(3.2a)

and

$$\frac{\partial h}{\partial t} + \nu h = -\sum_{m=1}^{N} x_m \mathcal{H}'(x - m\delta), \tag{3.2b}$$

where we have dropped the carets on the perturbed variables, and primes denote differentiation with respect to x.

The difficulty in analysing (3.2) rests in the temporal non-locality of the free-surface perturbation, h(x,t). To circumnavigate this issue and project the dynamics entirely onto the droplet trajectories, $x_n(t)$, we use the form of (3.2*b*) to define the auxiliary variables $\bar{x}_n(t)$ satisfying

$$\dot{\overline{x}}_n + \nu \overline{x}_n = x_n \quad \text{for } n = 1, \dots, N,$$
 (3.3)

a procedure that we also apply throughout the weakly nonlinear analysis presented in §4. It then follows from (3.2*b*) that the evolution of the perturbed free-surface elevation, h(x, t), may now be expressed in terms of the auxiliary variables, $\bar{x}_n(t)$. Specifically, we obtain the particular solution

$$h = -\sum_{m=-1}^{N} \mathcal{H}'(x - m\delta)\overline{x}_{m}.$$
(3.4)

The homogeneous solution to (3.2b) decays exponentially in time, and thus plays no role in either the linear or weakly nonlinear stability (§4) of the system. Having expressed h in terms of the auxiliary variables \bar{x}_n , we recast (3.2) as a reduced dynamical system for the variables x_n and \bar{x}_n .

Substituting (3.4) into (3.2*a*), and using (3.1), we find that $\mathcal{L}_n(x) = 0$, where $x = (x_1, \dots, x_N)$. The linear operator \mathcal{L}_n is defined as

$$\mathcal{L}_n(\mathbf{x}) = \ddot{\mathbf{x}}_n + \dot{\mathbf{x}}_n + \sum_{m=1}^N \left(\frac{\mathbf{x}_n}{\mathbf{v}} - \overline{\mathbf{x}}_m\right) \mathcal{H}''(\delta(n-m)),\tag{3.5}$$

which, together with equations (3.3), constitute a linear system of 2N ordinary differential equations describing the evolution of x_n from the steady state. Equations (3.3) and (3.5) may be solved using standard eigenmode methods, the periodicity of the steady lattice prompting the *ansatz*

$$x_n = A \exp(ikn\alpha + \lambda_k t) + \text{c.c.}, \quad \overline{x}_n = \frac{A}{\lambda_k + \nu} \exp(ikn\alpha + \lambda_k t) + \text{c.c.},$$
 (3.6)

where the form of \bar{x}_n follows from (3.3). (With \bar{x}_m written in the form (3.6), we note that (3.4) assumes a similar form to a Bloch wave.) Here, we have defined the angular spacing parameter $\alpha = 2\pi/N$, imaginary unit i, and complex amplitude A, where c.c. denotes complex conjugation of the preceding term. By symmetry considerations, we restrict our attention to the wavenumbers $k = 0, \ldots, \overline{N}$, where $\overline{N} = \lfloor N/2 \rfloor$. By substituting (3.6) into (3.5), we obtain the dispersion relation $\mathcal{D}_k(\lambda_k; \nu) = 0$, where

$$\mathcal{D}_k(\lambda; \nu) = \lambda^2 + \lambda + \frac{c_0}{\nu} - \frac{c_k}{\lambda + \nu}.$$
 (3.7)

The real constants c_k are defined as

$$c_k = \sum_{n=1}^{N} \cos(kn\alpha) \,\mathcal{H}''(n\delta),\tag{3.8}$$

which may be interpreted as the discrete cosine transform coefficients of the even and periodic function $\mathcal{H}''(x)$, arising from the discrete convolution in equation (3.5).

Upon rearranging $\mathcal{D}_k(\lambda_k; \nu) = 0$ and writing $\nu = 1/M$, the eigenvalues, λ_k , describing the asymptotic linear stability of (3.2), satisfy the cubic polynomial

$$M\lambda_k^3 + (M+1)\lambda_k^2 + (c_0M^2 + 1)\lambda_k + M(c_0 - c_k) = 0,$$
(3.9)

whose roots we typically compute numerically. The uniform lattice is asymptotically unstable if, for some wavenumber k, there exists an eigenvalue λ_k satisfying $\text{Re}(\lambda_k) > 0$. A fundamental property of this lattice is the rotational invariance, characterized by the eigenvalue $\lambda_0 = 0$, which may allow for a slow drift of the lattice in the weakly nonlinear regime (see §4).

It transpires that the lattice may destabilize via two distinct mechanisms: (i) a memory-independent instability, where the lattice wave field destabilizes the uniform configuration for all memory M > 0 (so $M_c = 0$); and (ii) a memory-driven instability when the wave force exceeds the drag force, prompting propulsion of the droplets for $M > M_c > 0$ (to be determined). Physically, case (i) arises from geometrical frustration of the lattice wave field: for particular

lattice configurations, the lattice wave field precludes the formation of a stable, equispaced lattice, forcing the droplets to occupy a nearby equilibrium configuration. Henceforth, we will thus refer to case (i) as a *geometric instability*. The memory-driven instability (ii) may be further decomposed into two subcategories: instability via a real eigenvalue, giving rise to the steady rotation of the lattice, analogous to the dynamics of a single walking droplet [38]; and oscillatory instabilities arising for droplets in close proximity, akin to those observed in experiments of this lattice system [25]. We discuss each of the foregoing cases and their implications in the following three sections.

(a) Geometric instability

For short memory $M \ll 1$ (equivalently, $\nu \gg 1$), the polynomial (3.9) admits three real roots:

$$\lambda_k^{(1)} = -1 + O(M), \quad \lambda_k^{(2)} = -\frac{1}{M} + O(1) \quad \text{and} \quad \lambda_k^{(3)} = (c_k - c_0)M + O(M^2).$$
 (3.10)

Thus, if there exists a wavenumber k_* such that $c_{k_*} > c_0$, then $\lambda_{k_*}^{(3)} > 0$ and the lattice is unconditionally unstable for $M \ll 1$. In fact, the lattice is unconditionally unstable for all M > 0 when $c_k > c_0$, the negativity of the constant term in (3.9) always giving rise to a positive real root. While the asymptotic results (3.10) provide a mathematical rationale for this memory-independent instability, they provide little in the way of physical intuition, which we presently provide.

We first introduce the rescaled variables $\tau = Mt$ and H = h/M and substitute into equations (2.5). We then consider the low-memory limit $M \ll 1$, leading us to neglect the highest-order time derivative in each equation. The result is overdamped, gradient-driven motion for each droplet described by

$$\frac{\mathrm{d}x_n}{\mathrm{d}\tau} = -\sum_{m=1}^{N} \mathcal{H}'(x_n - x_m),\tag{3.11}$$

where the wave field is $H(x,\tau) = \sum_{m=1}^{N} \mathcal{H}(x-x_m(\tau))$. If all but one of the droplets were static, then the remaining droplet would evolve in response to a fixed potential prescribed by the wave field. However, due to the spatially non-local coupling of the lattice, this motion in turn alters the wave force acting on all other droplets, prompting propulsion. As such, it is necessary to consider the global dynamics of the system.

We characterize the dynamics by the mean height of the wave field beneath each droplet

$$\mathcal{H}(\tau) = \frac{1}{N} \sum_{n=1}^{N} H(x_n(\tau), \tau) = \frac{1}{N} \sum_{n=1}^{N} \sum_{m=1}^{N} \mathcal{H}(x_n(\tau) - x_m(\tau)). \tag{3.12a}$$

Using (3.11) and that $\mathcal{H}(x)$ is an even, periodic function, it is readily verified that

$$\frac{\mathrm{d}\mathscr{H}}{\mathrm{d}\tau} = -\frac{2}{N} \sum_{n=1}^{N} \left(\frac{\mathrm{d}x_n}{\mathrm{d}\tau} \right)^2 \le 0, \tag{3.12b}$$

indicating that the mean wave height, \mathcal{H} , decreases along droplet trajectories (except at lattice equilibria). This phenomenon was also observed numerically in simulations of two-dimensional lattices [37]. Indeed, the foregoing argument readily generalizes to this latter case, and thus may be applied to this wider class of system [50–53].

We now provide an alternative interpretation of the geometric instability in terms of the energy-like quantity \mathcal{H} . When perturbing about the equispaced lattice, with $x_n(\tau) = n\delta + \eta \hat{x}_n(\tau)$ (with $0 < \eta \ll 1$), we compute the change in \mathcal{H} from the steady state $\mathcal{H}_0 = \sum_{n=1}^N \mathcal{H}(n\delta)$. By substituting this *ansatz* into (3.12*a*) and Taylor expanding in powers of η , we obtain

$$\mathcal{H} = \mathcal{H}_0 + \eta^2 \left[\frac{1}{N} \hat{\mathbf{x}}^T (c_0 \mathbf{I} - \mathbf{A}) \hat{\mathbf{x}} \right] + O(\eta^3),$$

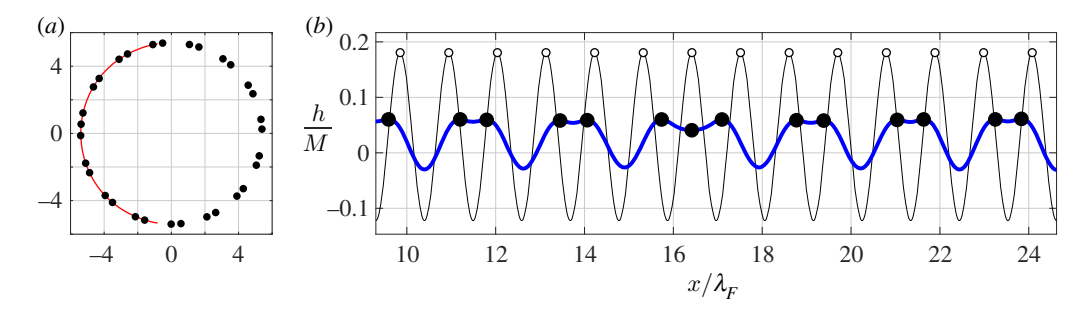


Figure 3. The onset of geometric instability in the low-memory regime for N=31 droplets. Black circles denote the final droplet rest state, a configuration that provides a local minimizer for the mean wave height \mathcal{H} (see (3.12)). (a) Overhead view of the final lattice, where lengths are normalized by the Faraday wavelength. (b) Initial (thin curve) and final (thick curve) lattice wave fields, h, plotted over the arc denoted by the red curve in (a). White circles denote the initial positions of the equispaced, unstable lattice. (Online version in colour.)

where $\hat{x} = (\hat{x}_1, \dots, \hat{x}_n)^T$, I is the identity matrix, and A is the symmetric, circulant matrix with entries $A_{nm} = \mathcal{H}''(\delta(n-m))$. The stability of the equispaced lattice thus depends entirely on the definiteness of the matrix $(c_0I - A)$, where negative eigenvalues indicate instability since \mathscr{H} can decrease in the direction of the corresponding eigenvector. Due to the form of A, its eigenvalues are c_k (for $k = 0, \dots, N-1$) with corresponding eigenvectors v_k whose nth element is $e^{ikn\alpha}$ (consistent with the normal modes ansatz in (3.6)). Hence, the energy may decrease if there exists k_* such that $c_0 - c_{k_*} < 0$ (recall (3.10)), rendering the steady lattice a saddle. When multiple wavenumbers satisfy this condition, the lattice rearranges in the direction of steepest descent of this energy-like quantity, \mathscr{H} , prescribed by the wavenumber k_* that minimizes $c_0 - c_k$. When N is even and $k_* = N/2$, symmetry dictates that the droplets approach a lattice whose separation distances alternate in size. For other values of k_* , more exotic, asymmetric lattice structures emerge, such as the 31-droplet lattice presented in figure 3. In fact, such an instability can even affect two well-separated droplets (specifically, $\delta \gg l$), despite the waves felt by the other droplet being exponentially small, emphasizing the extent of the spatially non-local coupling.

(b) Onset of collective walking

If the lattice configuration is not geometrically unstable, the system may destabilize to collective walking when the memory, M, increases above a critical threshold (to be determined). One such instability arises when a real eigenvalue of (3.9) passes through the origin, going from negative to positive. Such an instability typically arises when k=0 and λ_0 becomes a double eigenvalue at the instability threshold, although it is also possible in the exceptional case when there exists $k=k_*$ such that $c_{k_*}=c_0$ (since $\lambda_{k_*}=0$ is then also a trivial root of (3.9)). By factorizing (3.9) when $c_k=c_0$, the non-trivial eigenvalues satisfy the quadratic polynomial

$$M\lambda_0^2 + (M+1)\lambda_0 + (c_0M^2 + 1) = 0.$$
 (3.13)

Since M > 0, the stability of the system depends on the sign of the constant term in (3.13), where c_0 determines the local curvature beneath each droplet in the steady lattice.

When $c_0 < 0$, corresponding to each droplet sitting on a peak of the free surface, both roots of (3.13) are real. The system destabilizes at the critical threshold $M = 1/\sqrt{-c_0}$, at which one eigenvalue transitions from a stable node to a saddle, characteristic of a pitchfork bifurcation. Physically, this is the threshold at which the wave force dominates the drag force, promoting unidirectional self-propulsion, and thus is the many-droplet analogue of the walking threshold described in [38], for which a supercritical pitchfork bifurcation arises [30].

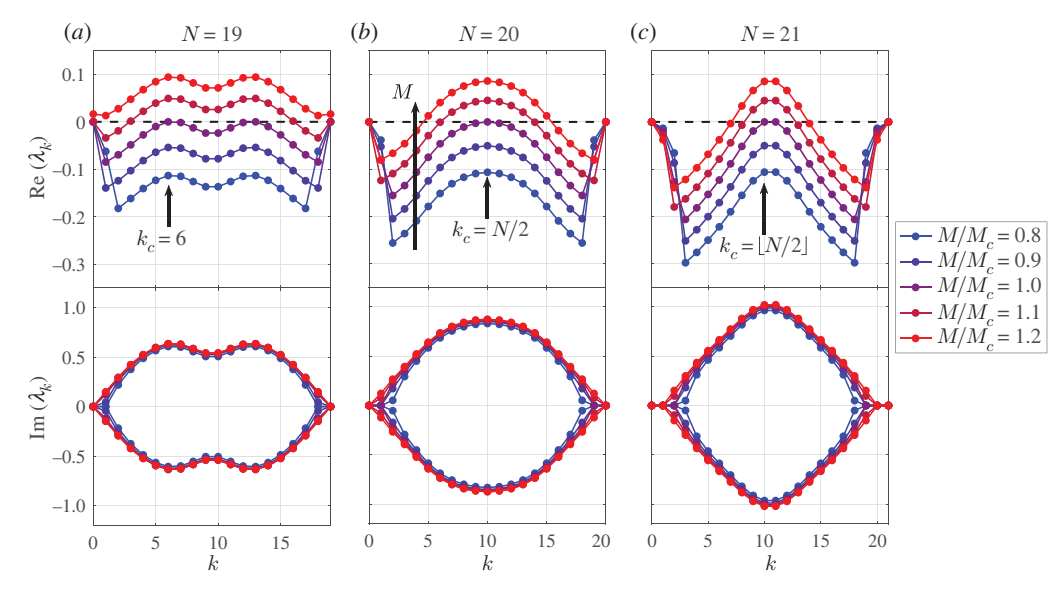


Figure 4. The real (top panel) and imaginary (bottom panel) parts of the dominant eigenvalues, λ_k , determined from the cubic polynomial (3.9) for (a) N=19, (b) N=20 and (c) N=21. As M is gradually increased, a single wavenumber $k_c \in [0, \overline{N}]$ touches $\text{Re}(\lambda_{k_c})=0$, while $\text{Im}(\lambda_{k_c})\neq 0$. The upper and lower branches correspond to one member of the conjugate pair. As M is increased further, yet more neighbouring wavenumbers destabilize about k_c . In contrast to N=20 and N=21, there is a notable departure of k_c from $k=\overline{N}$ when N=19, a hallmark of subcritical bifurcations (see §5). (Online version in colour.)

By contrast, when $c_0 > 0$, each droplet sits in a trough of the free surface, a highly stable configuration. As such, $\text{Re}(\lambda_0) < 0$ for all M, where the system may return to its rest state via either overdamped or underdamped oscillations. Such a regime may arise when the troughs about the central peak of the wave kernel, \mathcal{H} , are sufficiently deep (akin to the numerical examples presented in figure 2a and the electronic supplementary material) and the droplets lie in close proximity.

(c) Oscillatory instability

Of particular relevance to the experiments described in [25] is the case where the lattice undergoes instead an oscillatory instability, wherein the real part of a complex-conjugate pair of eigenvalues transitions from negative to positive as memory is increased (indicative, but not conclusive, of a Hopf bifurcation; see §4). We note that a lattice may have consecutive pitchfork and oscillatory instabilities as M is varied, in which case the form and threshold of the instability is determined by the smallest such critical M.

In figure 4, we demonstrate the possible forms of an oscillatory instability through consideration of the real and imaginary parts of the dominant eigenvalue, λ_k , for three consecutive droplet configurations: N=19, N=20 and N=21. As the memory, M, is increased, a single wavenumber $k_c \in [0, \overline{N}]$ touches $\text{Re}(\lambda_{k_c}) = 0$ for some critical value of $M = M_c$ (determined below), while $\text{Im}(\lambda_{k_c}) = \omega_{k_c} \neq 0$, corresponding to an oscillatory instability. As M is increased further, beyond M_c , yet more wavenumbers destabilize as their corresponding eigenvalues cross the imaginary axis. Of particular interest is the case N=20 (figure 4b), where the critical wavenumber is $k_c = N/2$ in the current parameter regime. According to the linear stability analysis, each droplet position is described by $x_n = n\delta + (-1)^n [A \exp(i\omega_{k_c}t) + \text{c.c.}]$ at $M = M_c$ in this case, corresponding to out-of-phase oscillations of adjacent droplets, akin to experimental observations [25, fig. 2]. We also observe a notable departure in k_c from $k = \overline{N}$ for N = 19 (figure 4a), contrasting with N = 20 and N = 21. This shift appears to be a hallmark of subcritical bifurcations (see §5). To fully describe

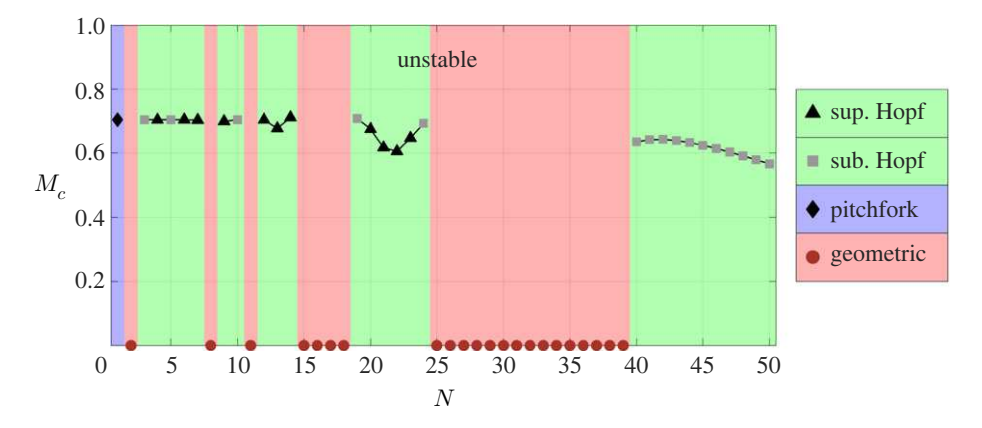


Figure 5. The critical instability threshold, M_c , as a function of the number of droplets, N, for a fixed ring radius $r_0 = 5.4$. The lattice is unstable when the memory parameter, $M = v^{-1}$, satisfies $M > M_c$, and is stable for $M < M_c$. The form of each instability is characterized by the legend. Black lines between data points are visual guides. (Online version in colour.)

the lattice dynamics for $M > M_c$, we consider the weakly nonlinear stability of these oscillations in §4.

At the critical threshold $M = M_k$, the memory at which wavenumber k goes unstable, the critical eigenvalue is $\lambda_k = i\omega_k$, where $\omega_k > 0$ without loss of generality. Upon substituting into (3.9) and taking real and imaginary parts, we obtain two equations for ω_k , namely

$$\omega_k^2 = c_0 M_k + \frac{1}{M_k}$$
 and $\omega_k^2 = \frac{M_k (c_0 - c_k)}{M_k + 1}$. (3.14)

By eliminating ω_k , we find that M_k satisfies $p(M_k) = 0$, where $p(M) = c_0 M^3 + c_k M^2 + M + 1$. We identify M_k as the smallest real root of p for each wavenumber k and define the critical lattice instability threshold as $M_c = \min_k M_k$, the minimum memory over all wavenumbers. The corresponding critical angular frequency $\omega_c = \omega_{k_c}$ may then be determined from (3.14), namely $\omega_c = \sqrt{c_0 M_c + 1/M_c}$.

(d) Summary

The form of each instability outlined in §3a–c is summarized in figure 5, where we present M_c for each droplet configuration consisting of N droplets. Lattice configurations are either geometrically unstable ($M_c = 0$), or instability is triggered by memory effects ($M_c > 0$) through a pitchfork bifurcation or an oscillatory instability. (Foreshadowing the results of §4, the oscillatory instabilities may be categorized as either supercritical or subcritical Hopf bifurcations.) We observe no apparent pattern in the distribution of memory-driven or geometric instabilities, principally due to the fact that N is varied discretely. As portrayed in §5, a more illuminating view is afforded when changing the lattice radius, r_0 , continuously and fixing N.

4. Weakly nonlinear oscillations and self-induced drift

The results of §3 suggest that, for geometrically stable lattice configurations (excluding the case N=1), the lattice destabilizes via a Hopf bifurcation. (Technically, these are not Hopf bifurcations in the strict sense, as—due to rotational invariance of the lattice—the fixed point is non-isolated.) In general, the Hopf bifurcation is one of two types: supercritical, in which stable, small-amplitude oscillations arise beyond the instability threshold, propelled by the slope of the droplet wave field (figure 6); or subcritical, where the system jumps to a distant attractor (such as a solitary-like wave [25]). We proceed to perform a weakly nonlinear analysis in the vicinity of the bifurcation point,

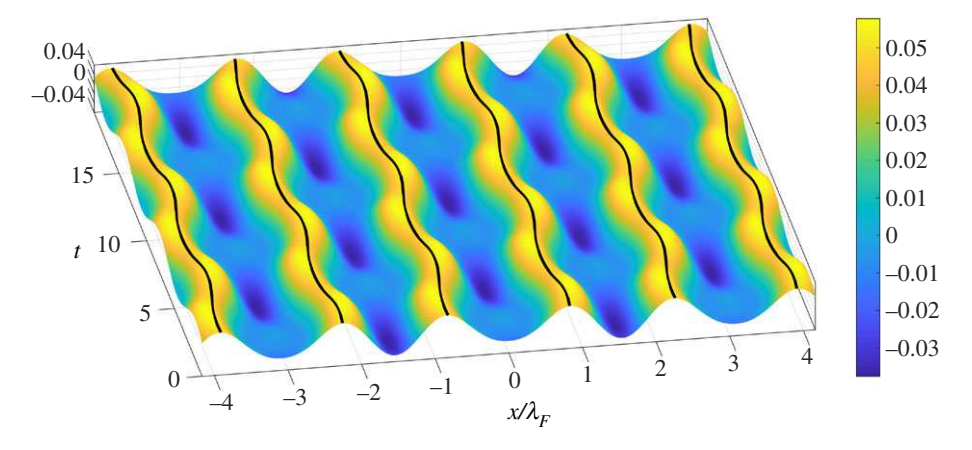


Figure 6. Surface plot of the evolution of the wave field, h, and droplet positions (black curves) for N=22 droplets, exhibiting out-of-phase oscillations slightly beyond the onset of a supercritical bifurcation (specifically, $\nu_c - \nu = 0.02$). (Online version in colour.)

 $v = v_c = 1/M_c$, allowing us to distinguish between these two contrasting dynamics of this spatially and temporally non-local system.

When ν is only slightly less than ν_c , we set $\nu_c - \nu = \varepsilon^2$, where $0 < \varepsilon \ll 1$, corresponding to M slightly above the critical threshold, M_c . We then pose the following asymptotic multiple-scales expansions:

$$x_n \sim n\delta + D(T) + \sum_{i=1}^{\infty} \varepsilon^i x_n^{(i)}(t, T) \quad \text{and} \quad h \sim \sum_{i=0}^{\infty} \varepsilon^i h^{(i)}(x, t, T),$$
 (4.1)

where $T = \varepsilon^2 t$ is the slow time scale. The O(1) drift, D(T), may give rise to a net rotation of the lattice. The origin of this drift may be traced back to the k = 0 mode of the dispersion relation (3.9), corresponding to translational invariance. (We note that the Stokes drift in surface gravity waves arises in a similar manner [54].) The asymptotic expansions (4.1) are standard for the method of multiple scales [55,56]. The fast time scale t characterizes the time scale of the unstable droplet oscillations beyond v_c , while T incorporates the slow amplitude modulation of the instability. We expect the expansions (4.1) to remain valid over long time scales, provided the amplitude of oscillations remains small, specifically of size $O(\varepsilon)$. The effects of neglected higher-order nonlinear terms only become significant when $T = O(1/\varepsilon)$.

The path memory stored within the free surface (entering through equation (2.5b)) means that the requisite calculations involved in this procedure are non-standard and (unfortunately) lengthy, with full details outlined in appendix A. Stated succinctly, the outcome of the multiple-scales analysis is that each droplet evolves according to

$$x_n = n\delta + [D(T) + O(\varepsilon)] + \varepsilon \left[A(T)e^{i(k_c n\alpha + \omega_c t)} + \text{c.c.} \right] + O(\varepsilon^2),$$

where the slowly varying complex amplitude A is governed by the Stuart–Landau equation

$$\frac{\mathrm{d}A}{\mathrm{d}T} = \gamma_1 A - \gamma_2 |A|^2 A. \tag{4.2}$$

The accompanying equation governing the evolution of the drift, *D*, is

$$\frac{\mathrm{d}D}{\mathrm{d}T} = \gamma_3 |A|^2. \tag{4.3}$$

The coefficients $\gamma_1, \gamma_2 \in \mathbb{C}$ and $\gamma_3 \in \mathbb{R}$ are defined in terms of the system parameters in appendix A. When the critical wavenumber of instability is $k_c = N/2$, corresponding to out-of-phase oscillations of the droplets (recall §3c), we find that $\gamma_3 = 0$ and hence D = constant. Otherwise

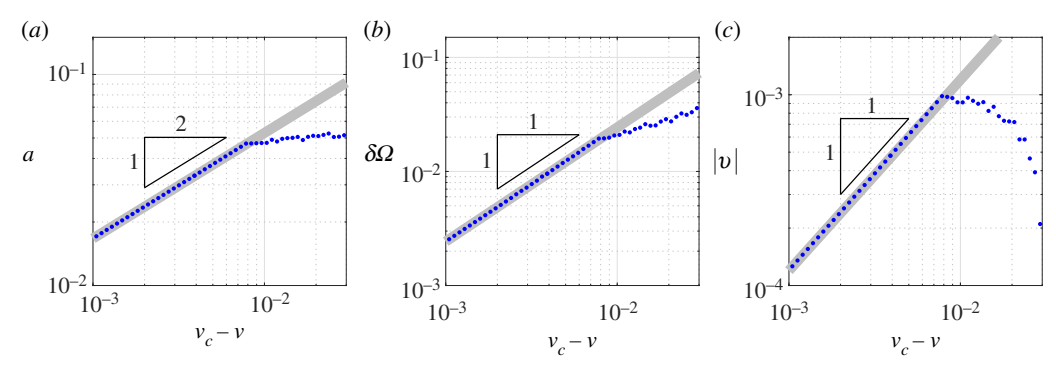


Figure 7. Numerical (blue dots) and analytical (grey) predictions of a supercritical Hopf bifurcation for N=23, as a function of $v_{\ell}-v=\varepsilon^2$. (a) The oscillation amplitude a. (b) The change in angular frequency $\delta \Omega=|\Omega-\omega_{\ell}|$. (c) The drift speed |v|. All numerical results were obtained by simulating (2.5) until a constant-amplitude, periodic state was attained. The numerical and analytical predictions are virtually superimposed when ε is sufficiently small: as ε increases, however, the oscillations undergo a second bifurcation, beyond which the dynamics become chaotic in this case. (Online version in colour.)

the lattice is endowed with a non-zero drift velocity superimposed on top of individual droplet oscillations, a phenomenon also observed in free-space rings [37]. Furthermore, we observe from (4.3) that when |A| is constant, D is linear in T and the lattice rotates with constant speed.

Furnished with equation (4.2), we now specify to which variety of Hopf bifurcation each lattice configuration destabilizes. By recasting A in (4.2) in polar form $A = \rho \exp(i\phi)$ (where $\rho(T) \ge 0$ and $\phi(T)$ are both real) and equating real and imaginary parts, we find

$$\frac{\mathrm{d}\rho}{\mathrm{d}T} = r_1 \rho - r_2 \rho^3 \tag{4.4}$$

and

$$\frac{\mathrm{d}\phi}{\mathrm{d}T} = s_1 - s_2 \rho^2,\tag{4.5}$$

where $r_i = \text{Re}(\gamma_i)$ and $s_i = \text{Im}(\gamma_i)$. Consistent with the linear stability analysis performed in §3, r_1 satisfies $r_1 > 0$, rendering the fixed point $\rho = 0$ (corresponding to a stationary lattice) unstable. If $r_2 > 0$, there is a second, stable, fixed point $\rho_* = \sqrt{r_1/r_2}$, corresponding to a supercritical Hopf bifurcation. From (4.5), the corresponding phase is $\phi(T) = \phi_* T$ where $\phi_* = s_1 - s_2 r_1/r_2$ (we set the constant of integration, corresponding to an arbitrary phase-shift, to zero by temporal invariance). Conversely, if $r_2 < 0$ then no additional fixed points emerge beyond the instability threshold, characteristic of a subcritical bifurcation.

We return our attention to figure 5, in which we mark supercritical $(r_2 > 0)$ and subcritical $(r_2 < 0)$ Hopf bifurcations for varying N. Although the precise details of this figure depend on the form of the wave kernel, \mathcal{H} , we see that it portrays one of the fundamental features of the experiments [25], namely the transition from a super- to subcritical Hopf bifurcation as the number of droplets is doubled from N = 20 to N = 40. Physically, stable, small-amplitude oscillations arise for $M > M_c$ when the Hopf bifurcation is supercritical, yet a distant attractor is approached for a subcritical Hopf bifurcation (which, in experiments, takes the form of a solitary wave [25]). The subtle implications of instead varying the ring radius, r_0 , while keeping the number of droplets, N, fixed, are discussed in §5.

Finally, we justify the efficacy of (4.2) and (4.3) in describing the dynamics of the system (2.5) beyond a supercritical bifurcation point. There is a stable, periodic regime in which each droplet

$$x_n(t) = n\delta + d(t) + a\cos(\Omega t + \Psi_n) + O(\varepsilon^2),$$

where the drift $d(t) = v(t - t_0) + O(\varepsilon)$ proceeds with velocity $v = \gamma_3(r_1/r_2)(v_c - v)$. The amplitude of the oscillations is $a = 2\rho_*\sqrt{v_c - v}$ and $\Omega = \phi_*(v_c - v) + \omega_c$ is the angular frequency. Each oscillation has an associated phase shift $\Psi_n = k_c n\alpha$.

In figure 7, we compare direct numerical simulations of (2.5) with our predictions for a, Ω , and v in the supercritical case N=23. Our numerical solutions were computed using a Fourier spectral method, with code and documentation provided in the electronic supplementary material. For $0 < v_c - v \ll 1$, our analytical and numerical predictions are virtually superimposed. If $v_c - v$ becomes too large, however, a significant discrepancy arises, which we attribute to the onset of a second bifurcation wherein the oscillations themselves destabilize. It is then necessary to take into account spatial, as well as temporal, variations of the amplitude A(T), which will be explored elsewhere [57].

5. Control of stability

When the lattice radius, r_0 , is fixed and the number of droplets, N, is varied discretely, figure 5 shows no discernible pattern in the distribution of geometric and memory-driven instabilities. However, the discrete variation of N accounts only for a finite subset of the infinite family of possible droplet separations. To elucidate the underlying structure of the geometric and memory-driven instabilities, we instead consider how the stability of a lattice of N=20 droplets changes as r_0 is varied continuously. Herein, we characterize the dynamics by the dimensionless separation distance, $\delta = \Lambda/N = 2\pi r_0/N$. As we shall see, regions of geometric and memory-driven instability, in fact, arise quasi-periodically when δ is increased, with a period close to the Faraday wavelength. (We recall that all lengths are normalized by λ_F .) We note that the wave kernel, $\mathcal{H}(x)$, depends on r_0 through equation (2.6).

(a) Geometric instability

We first study the origins of geometric instability, which we recall from §3a occurs if there exists an integer k_* such that $c_{k_*} > c_0$. To aid the following discussion, we plot the coefficients c_k for $k \in [0, \overline{N} = 10]$ in figure 8c as a function of δ . The oscillatory form of the coefficients c_k with increasing δ (or r_0) arises due to the quasi-monochromatic form of $\mathcal{H}(x)$, the oscillation length scale being close to the Faraday wavelength (unity in dimensionless units). Moreover, c_0 and $c_{\overline{N}}$ tend to oscillate out of phase and bound the oscillations of $c_1,\ldots,c_{\overline{N}-1}$. The result is that regions of geometric instability typically begin and end at those values of δ where $c_{\overline{N}}$ crosses c_0 from below and above, respectively, thus selecting $k_* = \overline{N}$. Moreover, each successive region of geometric instability is separated by a Faraday wavelength ($\delta \approx 1$). This effect is preserved even when the droplets are well separated and interact weakly, specifically when δ greatly exceeds the wave kernel's decay length ($\delta \gg l$). In this limit, the coefficients c_k decay exponentially (to the asymptotic value $\mathcal{H}''(0)$, that of a single isolated droplet) over a length scale close to l, yet remain oscillatory.

(b) Memory-driven instability

In intervals of δ where the system undergoes a memory-driven Hopf bifurcation, figure 8a demonstrates that the instability threshold, M_c , varies smoothly, except at points where k_c switches between different integer values (figure 8b). It appears that the Hopf bifurcation is supercritical *only* when k_c is \overline{N} or $\overline{N}-1$ and subcritical otherwise (recall figure 4). When the droplets lie less than a Faraday wavelength apart ($\delta \lesssim 1$), the supercriticality region is very narrow, explaining the prevalence of subcritical bifurcations when the droplets are tightly packed. We note that for $\delta \lesssim 0.7$ in the current parameter regime (figure 8d), the steady lattice wave field exhibits

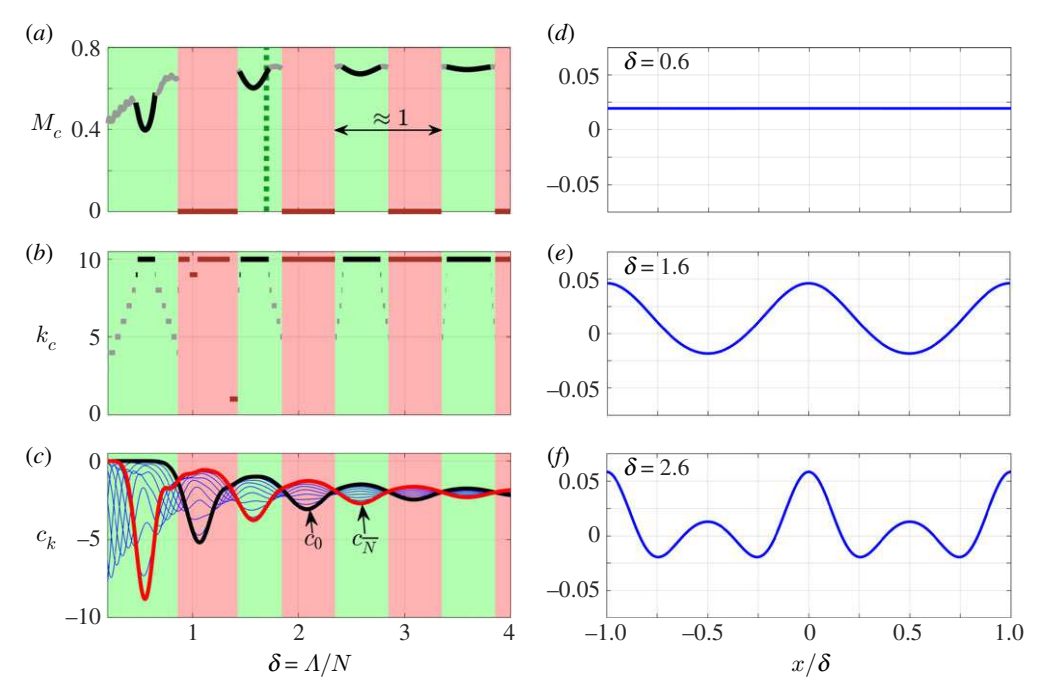


Figure 8. Delineation of the instability form when N=20 is fixed and the dimensionless ring radius, $r_0=\Lambda/(2\pi)$, is varied, altering the dimensionless separation distance, $\delta=\Lambda/N$. In (a-c), green and red backgrounds correspond to memory-driven $(M_c>0)$ and geometric instabilities $(M_c=0)$, respectively. (a) The critical memory, M_c , where the lattice is unstable for $M>M_c$. Kinks in M_c correspond to jumps in k_c . The dashed curve (dark green) corresponds to the N=20 instability in figure 5. (b) The corresponding critical wavenumber, k_c . For subcritical bifurcations, there is a notable departure in k_c from $k=\overline{N}$, an apparent hallmark of such configurations. In both (a) and (b), black and grey curves denote super- and subcritical Hopf bifurcations, respectively. Dark red lines correspond to geometric instability. (c) The coefficients c_k (blue curves), where c_0 and $c_{\overline{N}}=c_{10}$ are highlighted in black and red, respectively. (d-f) Steady lattice wave field centred beneath a droplet, extending to the two neighbouring droplets at $x=\pm\delta$, for (d) $\delta=0.6$, (e) $\delta=1.6$ and (f) $\delta=2.6$, all corresponding to supercritical Hopf bifurcations. When the droplets are packed tightly together, oscillations in the steady wave field become imperceptible. (Online version in colour.)

imperceptible oscillations, which present a marked contrast to when $\delta \gtrsim 1$ (figure $8e_f$), for which supercritical Hopf and geometric instabilities are prevalent.

(c) Summary

The regions of geometric instability thus provide quantized separation distances prescribed by the Faraday wavelength at which oscillations arise beyond the instability threshold. Moreover, we infer that subcritical bifurcations (and hence solitary-like waves) are more likely to arise when the droplets are either packed closely together ($\delta \lesssim 1$) or when δ is near the boundaries of geometric instability. However, the solitary wave dynamics are not captured by our highly simplified model, likely due to the omission of several potentially significant fluid mechanical effects that arise in this regime (see §2). Nevertheless, the foregoing observations are entirely consistent with experiments [25], where small-amplitude, out-of-phase oscillations and solitary-like waves are observed when the droplet spacings are around $1.8\lambda_F$ and $0.9\lambda_F$, respectively. Finally, the foregoing results point to the sensitivity of the experimental system [25]: we infer from figure 8 that a small change in ring radius, r_0 , or the addition/subtraction of a droplet may adversely affect the stability of the lattice, for example by pushing the lattice into a region of geometric instability.

6. Conclusion

In this paper, we considered the onset and stability of collective vibrations in an inertial active hydrodynamic lattice. This new class of dynamical oscillator is characterized by two features atypical of traditional oscillator systems: spatially non-local coupling, mediated in this case by the droplet wave field; and memory-driven self-propulsion of the lattice components. A consequence of the spatially non-local coupling is the possibility of geometric instability, where the lattice wave field acts to propel the droplets for all values of the memory parameter, M. Otherwise, linear stability predicts that the system typically destabilizes to an oscillatory instability beyond a critical memory.

The fate of the system close to the point of instability was then studied via a systematic weakly nonlinear analysis. At the onset of a memory-driven instability, the lattice system undergoes a Hopf bifurcation, which can be either supercritical, prompting stable, small-amplitude oscillations beyond the instability threshold, or subcritical, where the system jumps to a distant attractor, manifest in experiments as the excitation of a solitary-like wave [25]. In the supercritical regime, an oscillatory-rotary motion may arise from asymmetric droplet oscillations, a phenomenon observed in confined and free-space rings [25,37]. Moreover, when the lattice radius was fixed, our weakly nonlinear analysis corroborated one of the fundamental features of the experiments [25], namely the transition from a super- to subcritical Hopf bifurcation as the number of droplets was doubled from 20 to 40.

The dependence of the stability of the lattice on the system parameters was probed yet further when we allowed the lattice radius to vary continuously, while keeping the number of droplets fixed. Here, we found quantized separation distances similar in size to the Faraday wavelength, separating successive regions of geometric and memory-driven instability. Generalizing our result of the transition from a super- to subcritical Hopf bifurcation, we infer that subcritical bifurcations are more likely to arise when droplets are more tightly bound (less than a Faraday wavelength apart), while supercritical and geometric instabilities prevail when the droplet spacing is increased. These observations are consistent with the experimental results obtained for the droplet spacings reported in [25].

The potential avenues for investigation prompted by the results of this paper are numerous, and so we name only a few of the most salient here. Perhaps the most demanding is a description of the fully nonlinear dynamics of the solitary wave regime, specifically extending our model to consider variations in the droplets' vertical bouncing phase [43], or two-dimensional effects imposed by the geometry of the submerged annular channel [44]. Indeed, the fact that the wave force vanishes for tightly packed, equispaced lattices (figure 8*d*) is a portent that the simplified model (2.5) is insufficient to capture the solitary wave dynamics. Inspired by mathematical models of traffic flow [58], another avenue is to course-grain the discrete model (2.5) to derive a system of partial differential equations for the macroscopic droplet density and velocity. Such models provide a natural framework in which to study the propagation of nonlinear waves.

Our system also begs further attention when viewed as a dynamical system. In the future [57], we will show that taking into account spatial variations in the droplet oscillation amplitude, A, generalizes equation (4.2) to a complex Ginzburg–Landau equation, allowing us to rationalize the onset of the second bifurcation alluded to in figure 7. The techniques employed in this study may also, in principle, be extended to two-dimensional lattices [37,50–53]. Finally, the spatio-temporal non-locality present in our system also renders it a tantalizing experimental and theoretical candidate to investigate so-called chimera states in coupled oscillators [32–34,59–61].

Data accessibility. The code and documentation for the spectral implementation of the model (2.5) are provided in the electronic supplementary material.

Authors' contributions. S.J.T. conceived the research. S.J.T and M.D. constructed the model in §2 and carried out the analysis in §83–5, in consultation with R.R.R. M.D. wrote and implemented the spectral method for the model (2.5) and generated figures 2–8. All three authors contributed to writing the manuscript and gave final approval for publication, agreeing to each be held accountable for the work performed therein.

Competing interests. We declare we have no competing interests.

Funding. R.R.R. is partially supported by the National Science Foundation through grant no. DMS-1719637. Acknowledgements. The authors thank Daniel Harris (Brown University) for providing the picture used in figure 1a.

Appendix A. Derivation of the Stuart—Landau and drift equations

In this appendix, we provide details of the multiple-scales expansion leading to the amplitude and drift equations (4.2) and (4.3). The basic recipe is thus: first, we substitute the asymptotic expansions (4.1) into the stroboscopic model (2.5) and gather successive powers of ε . At each order, we suppress resonant terms (those that are either constant in t or proportional to $e^{i\phi_n(t)}$, where $\phi_n = k_c n\alpha + \omega_c t$), which are thereby solutions of the linear problem (3.5). This step is facilitated by introducing auxiliary variables to solve for the free surface h, akin to §3. This procedure gives rise to the Stuart–Landau equation (4.2) at $O(\varepsilon^3)$ and the drift equation (4.3) at $O(\varepsilon^2)$.

At leading order, we obtain a similar system to (3.1)

$$\frac{\partial h^{(0)}}{\partial x}\Big|_{x=x_n^{(0)}} = 0, \quad h^{(0)}(x,T) = \frac{1}{\nu_c} \sum_{m=1}^N \mathcal{H}(x - x_m^{(0)}),$$
 (A 1)

where $x_n^{(0)} = x_n^{(0)}(T) = n\delta + D(T)$. By symmetry of $h^{(0)}$, all odd-derivatives vanish beneath each droplet at equilibrium, a fact we will make repeated use of in simplifying forthcoming terms in our expansion.

At $O(\varepsilon)$, we obtain an analogous problem to (3.2) for $x_n^{(1)}$ and $h^{(1)}$. Hence, after defining the auxiliary variables X_n satisfying

$$\frac{\partial X_n}{\partial t} + \nu_c X_n = x_n^{(1)},$$

we obtain the particular solution

$$h^{(1)} = -\sum_{m=1}^{N} X_m \mathcal{H}'(x - x_m^{(0)}), \tag{A 2}$$

and $\mathcal{L}_n x^{(1)} = 0$, where the definition of the linear operator, \mathcal{L}_n , is the same as in (3.5) (with $\nu = \nu_c$) and $x^{(1)} = (x_1^{(1)}, \dots, x_N^{(1)})$. (Recall that the homogeneous part of $h^{(1)}$ decays exponentially in time (§3).) We now seek a solution to $\mathcal{L}_n x^{(1)} = 0$ of the form

$$x_n^{(1)} = B(T) + \left[A(T)e^{i\phi_n} + \text{c.c.} \right], \quad X_n = \frac{1}{\nu_c}B(T) + \left[\frac{A(T)}{\nu_c + i\omega_c}e^{i\phi_n} + \text{c.c.} \right],$$
 (A 3)

where *A* is a complex amplitude and *B* is a correction to the drift, *D*. This solution may be verified by recalling that the dispersion relation, \mathcal{D}_k , satisfies $\mathcal{D}_{k_c}(i\omega_c; \nu_c) = 0$ and $\mathcal{D}_0(0; \nu) = 0$.

At $O(\varepsilon^2)$, we have the following system for $x_n^{(2)}$ and $h^{(2)}$:

$$\frac{\partial^{2} x_{n}^{(2)}}{\partial t^{2}} + \frac{\partial x_{n}^{(2)}}{\partial t} + \frac{\mathrm{d}D}{\mathrm{d}T} = -\left\{ \frac{\partial h^{(2)}}{\partial x} + x_{n}^{(2)} \frac{\partial^{2} h^{(0)}}{\partial x^{2}} + x_{n}^{(1)} \frac{\partial^{2} h^{(1)}}{\partial x^{2}} \right\} \Big|_{x = x_{n}^{(0)}} \tag{A 4}$$

$$\frac{\partial h^{(2)}}{\partial t} + v_c h^{(2)} + \frac{\partial h^{(0)}}{\partial T} = h^{(0)} + \sum_{m=1}^{N} \left\{ \frac{1}{2} x_m^{(1)2} \mathcal{H}''(x - x_m^{(0)}) - x_m^{(2)} \mathcal{H}'(x - x_m^{(0)}) \right\}. \tag{A 5}$$

To solve for $h^{(2)}$, we introduce two further auxiliary variables, Y_n and Z_n , akin to the procedure adopted in (3.3). By the form of the inhomogeneity in (A 5), we pose that Y_n and Z_n satisfy

$$\frac{\partial Y_n}{\partial t} + \nu_c Y_n = \frac{1}{2} x_n^{(1)2} \quad \text{and} \quad \frac{\partial Z_n}{\partial t} + \nu_c Z_n = x_n^{(2)}. \tag{A 6}$$

A particular solution of (A 5) is then found:

$$h^{(2)} = \frac{1}{\nu_c} \left(h^{(0)} - \frac{\partial h^{(0)}}{\partial T} \right) + \sum_{m=1}^{N} \left\{ Y_m \mathcal{H}''(x - x_m^{(0)}) - Z_m \mathcal{H}'(x - x_m^{(0)}) \right\}. \tag{A 7}$$

Using the form of $x_n^{(1)}$, we find from the first equation in (A 6) that

$$Y_n = \frac{1}{\nu_c} \left[|A|^2 + \frac{1}{2}B^2 \right] + B \left[\frac{A}{\nu_c + i\omega_c} e^{i\phi_n} + c.c. \right] + \frac{1}{2} \left[\frac{A^2}{\nu_c + 2i\omega_c} e^{2i\phi_n} + c.c. \right].$$
 (A 8)

Substituting (A 7) and (A 8) into (A 4), and using (A 1), then yields

$$\mathcal{L}_n \mathbf{x}^{(2)} = -\alpha_0 \frac{\mathrm{d}D}{\mathrm{d}T} + \left\{ a_1 A^2 e^{2i\phi_n} + \text{c.c.} \right\} + a_2 |A|^2, \tag{A 9}$$

where the coefficients α_0 , a_1 and a_2 are included in the summary at the end of this appendix.

For a bounded solution of (A 9), we require that the constant secular terms on the right-hand side vanish, yielding an equation governing the drift *D*:

$$\alpha_0 \frac{\mathrm{d}D}{\mathrm{d}T} = a_2 |A|^2. \tag{A 10}$$

As terms proportional to $e^{\pm 2i\phi_n(t)}$ in (A 9) are non-secular, the general solution of (A 9) is then

$$x_n^{(2)} = \left[C(T)e^{i\phi_n} + \text{c.c.} \right] + \left[\frac{a_1 A^2}{\mathcal{D}_{2k_c}(2i\omega_c; \nu_c)} e^{2i\phi_n} + \text{c.c.} \right] + E(T),$$

where *C* and *E* are corrections to the complex amplitude, *A*, and drift, *D*, respectively. Thus, from the second equation in (A 6), we find

$$Z_n = \left[\frac{\tilde{a}_1 A^2}{\nu_c + 2i\omega_c} e^{2i\phi_n} + \text{c.c.} \right] + \left[\frac{C}{\nu_c + i\omega_c} e^{i\phi_n} + \text{c.c.} \right] + \frac{1}{\nu_c} E, \quad \text{where} \quad \tilde{a}_1 = \frac{a_1}{\mathcal{D}_{2k_c}(2i\omega_c; k_c)}.$$

At $O(\varepsilon^3)$, we have a system for $x_n^{(3)}$ and $h^{(3)}$, namely

$$\begin{split} &\frac{\partial^{2} x_{n}^{(3)}}{\partial t^{2}}+\frac{\partial x_{n}^{(3)}}{\partial t}+x_{n}^{(3)}\frac{\partial^{2} h^{(0)}}{\partial x^{2}}\bigg|_{x=x_{n}^{(0)}}=-\left[2\frac{\partial^{2} x_{n}^{(1)}}{\partial t \partial T}+\frac{\partial x_{n}^{(1)}}{\partial T}\right]\\ &-\left[\frac{\partial h^{(3)}}{\partial x}+x_{n}^{(1)}\frac{\partial^{2} h^{(2)}}{\partial x^{2}}+\frac{1}{2}x_{n}^{(1)2}\frac{\partial^{3} h^{(1)}}{\partial x^{3}}+x_{n}^{(2)}\frac{\partial^{2} h^{(1)}}{\partial x^{2}}+\frac{1}{6}x_{n}^{(1)3}\frac{\partial^{4} h^{(0)}}{\partial x^{4}}\right]\bigg|_{x=x_{n}^{(0)}} \end{split} \tag{A 11}$$

and

$$\frac{\partial h^{(3)}}{\partial t} + \nu_c h^{(3)} = -\left[\frac{\partial h^{(1)}}{\partial T} - h^{(1)}\right]
+ \sum_{m=1}^{N} \left\{ x_m^{(1)} x_m^{(2)} \mathcal{H}''(x - x_m^{(0)}) - x_m^{(3)} \mathcal{H}'(x - x_m^{(0)}) - \frac{1}{6} x_m^{(1)3} \mathcal{H}'''(x - x_m^{(0)}) \right\}.$$
(A 12)

In an identical procedure to that carried out at $O(\varepsilon^2)$, introducing three further auxiliary variables allows us to find a particular solution of (A 12) governing $h^{(3)}$. Then, after substituting $h^{(3)}$ into (A 11), eliminating secular terms (either constant in t or proportional to $e^{i\phi_n(t)}$) yields two equations governing the complex amplitude, A, and real drift, B, namely

$$\alpha_1 \frac{\mathrm{d}A}{\mathrm{d}T} = \alpha_2 A - \alpha_3 |A|^2 A \tag{A 13}$$

and

$$\alpha_0 \frac{\mathrm{d}B}{\mathrm{d}T} = 2a_2 \,\mathrm{Re}[A^*C],\tag{A 14}$$

in addition to equation (A 10) governing the drift, D. The notation A^* denotes the complex conjugate of A. We cannot determine the higher-order corrections B, C and E without proceeding

to $O(\varepsilon^4)$ and higher. Nevertheless, a satisfactory approximation is obtained by considering A and D alone, as made clear by figure 7.

We conclude by summarizing the coefficients, where it helps to recall that $\mathcal{D}_k(\lambda; \nu)$ is the dispersion relation (3.7). For convenience, we introduce the notation $\mathcal{H}_n = \mathcal{H}(n\delta)$ (and similarly for derivatives). The coefficients α_0 , a_1 and a_2 appearing in (A 9), (A 10) and (A 14) are

$$\begin{split} &\alpha_0 = \frac{\partial \mathcal{D}_0}{\partial \lambda}(0; \nu_c) = 1 + \frac{1}{\nu_c^2} \sum_{n=1}^N \mathcal{H}_{n}^{\prime\prime}, \\ &a_1 = \frac{1}{\nu_c + i\omega_c} \sum_{n=1}^N e^{-ik_c n\alpha} \mathcal{H}_{n}^{\prime\prime\prime} - \frac{1}{2(\nu_c + 2i\omega_c)} \sum_{n=1}^N e^{-2ik_c n\alpha} \mathcal{H}_{n}^{\prime\prime\prime} \\ &a_2 = 2 \text{Re} \left[\frac{1}{\nu_c + i\omega_c} \sum_{n=1}^N e^{-ik_c n\alpha} \mathcal{H}_{n}^{\prime\prime\prime} \right] = -\frac{2\omega_c}{\nu_c^2 + \omega_c^2} \sum_{n=1}^N \sin(k_c n\alpha) \mathcal{H}_{n}^{\prime\prime\prime}, \end{split}$$

and

while the α_i , for i = 1, 2, 3, appearing in (A 13) are

$$\alpha_1 = \frac{\partial \mathcal{D}_{k_c}}{\partial \lambda}(i\omega_c; \nu_c), \quad \alpha_2 = \frac{\partial \mathcal{D}_{k_c}}{\partial \nu}(i\omega_c; \nu_c)$$

and

$$\begin{split} \alpha_{3} &= \frac{3}{2\nu_{c}} \sum_{n=1}^{N} \mathcal{H}_{n}'''' - \sum_{n=1}^{N} \mathcal{H}_{n}'''' \text{Re} \bigg[\frac{\mathrm{e}^{-\mathrm{i}k_{c}n\alpha}}{\nu_{c} + \mathrm{i}\omega_{c}} \bigg] + \frac{1}{2} \sum_{n=1}^{N} \frac{\mathcal{H}_{n}'''' \mathrm{e}^{-2\mathrm{i}k_{c}n\alpha}}{\nu_{c} + 2\mathrm{i}\omega_{c}} - \sum_{n=1}^{N} \frac{\mathcal{H}_{n}'''' \mathrm{e}^{-\mathrm{i}k_{c}n\alpha}}{\nu_{c} + \mathrm{i}\omega_{c}} \\ &+ 2\mathrm{i}\tilde{a}_{1} \sum_{n=1}^{N} \mathcal{H}_{n}''' \text{Im} \bigg[\frac{\mathrm{e}^{-\mathrm{i}k_{c}n\alpha}}{\nu_{c} + \mathrm{i}\omega_{c}} \bigg] - \tilde{a}_{1} \sum_{n=1}^{N} \frac{\mathcal{H}_{n}''' \mathrm{e}^{-2\mathrm{i}k_{c}n\alpha}}{\nu_{c} + 2\mathrm{i}\omega_{c}} - \frac{a_{2}}{\alpha_{0}} \sum_{n=1}^{N} \frac{\mathrm{e}^{-\mathrm{i}k_{c}n\alpha}\mathcal{H}_{n}'''}{(\nu_{c} + \mathrm{i}\omega_{c})^{2}}. \end{split}$$

Recall that $\tilde{a}_1 = a_1/\mathcal{D}_{2k_c}(2i\omega_c; \nu_c)$. On dividing (A 13) by α_1 and (A 10) by α_0 we arrive at equations (4.2) and (4.3) in the main text, where $\gamma_1 = \alpha_2/\alpha_1$, $\gamma_2 = \alpha_3/\alpha_1$, and $\gamma_3 = a_2/\alpha_0$. We note that when $k_c = N/2$, simplifications arise since $\tilde{a}_1 = a_1 = a_2 = 0$.

References

- 1. Ramaswamy S. 2010 The mechanics and statistics of active matter. *Annu. Rev. Condens. Matter Phys.* **1**, 323–345. (doi:10.1146/annurev-conmatphys-070909-104101)
- 2. Marchetti MC, Joanny JF, Ramaswamy S, Liverpool TB, Prost J, Rao M, Simha RA. 2013 Hydrodynamics of soft active matter. *Rev. Mod. Phys.* **85**, 1143–1189. (doi:10.1103/RevModPhys.85.1143)
- 3. Dunkel J, Heidenreich S, Drescher K, Wensink HH, Bär M, Goldstein RE. 2013 Fluid dynamics of bacterial turbulence. *Phys. Rev. Lett.* **110**, 228102. (doi:10.1103/PhysRevLett.110.228102)
- 4. Saintillan D, Shelley MJ. 2013 Active suspensions and their nonlinear models. *C.R. Phys.* 14, 497–517. (doi:10.1016/j.crhy.2013.04.001)
- 5. Bricard A, Caussin JB, Desreumaux N, Dauchot O, Bartolo D. 2013 Emergence of macroscopic directed motion in populations of motile colloids. *Nature* **503**, 95–98. (doi:10.1038/nature12673)
- 6. Bricard A *et al.* 2015 Emergent vortices in populations of colloidal rollers. *Nat. Commun.* **6**, 7470. (doi:10.1038/ncomms8470)
- 7. Souslov A, Van Zuiden BC, Bartolo D, Vitelli V. 2017 Topological sound in active-liquid metamaterials. *Nat. Phys.* **13**, 1091–1094. (doi:10.1038/nphys4193)
- 8. Geyer D, Morin A, Bartolo D. 2018 Sounds and hydrodynamics of polar active fluids. *Nat. Mater.* **17**, 789–793. (doi:10.1038/s41563-018-0123-4)

- 9. Beatus T, Tlusty T, Bar-Ziv R. 2006 Phonons in a one-dimensional microfluidic crystal. *Nat. Phys.* **2**, 743–748. (doi:10.1038/nphys432)
- Baron M, Bławzdziewicz J, Wajnryb E. 2008 Hydrodynamic crystals: collective dynamics of regular arrays of spherical particles in a parallel-wall channel. *Phys. Rev. Lett.* 100, 174502. (doi:10.1103/PhysRevLett.100.174502)
- Janssen P, Baron M, Anderson P, Blawzdziewicz J, Loewenberg M, Wajnryb E. 2012 Collective dynamics of confined rigid spheres and deformable drops. Soft Matter 8, 7495–7506. (doi:10.1039/c2sm25812a)
- 12. Schiller UD, Fleury JB, Seemann R, Gompper G. 2015 Collective waves in dense and confined microfluidic droplet arrays. *Soft Matter* 11, 5850–5861. (doi:10.1039/C5SM01116G)
- 13. Tsang ACH, Shelley MJ, Kanso E. 2018 Activity-induced instability of phonons in 1D microfluidic crystals. *Soft Matter* **14**, 945–950. (doi:10.1039/C7SM01335C)
- 14. Sáenz PJ, Pucci G, Goujon A, Cristea-Platon T, Dunkel J, Bush JWM. 2018 Spin lattices of walking droplets. *Phys. Rev. Fluids* 3, 100508. (doi:10.1103/PhysRevFluids.3.100508)
- 15. Sáenz PJ, Pucci G, Turton SE, Goujon A, Rosales RR, Dunkel J, Bush JWM. Submitted. Emergent order in hydrodynamic spin lattices.
- 16. Ebeling W, Erdmann U, Dunkel J, Jenssen M. 2000 Nonlinear dynamics and fluctuations of dissipative Toda chains. J. Stat. Phys. 101, 443–457. (doi:10.1023/A:1026407415248)
- 17. Makarov VA, Ebeling W, Velarde MG. 2000 Soliton-like waves on dissipative Toda lattices. *Int. J. Bifurcation Chaos* **10**, 1075–1089. (doi:10.1142/S0218127400000761)
- 18. Dunkel J, Ebeling W, Erdmann U, Makarov VA. 2002 Coherent motions and clusters in a dissipative Morse ring chain. *Int. J. Bifurcation Chaos* **12**, 2359–2377. (doi:10.1142/S0218127402005923)
- 19. Nekorkin VI, Velarde MG. 2012 Synergetic phenomena in active lattices: patterns, waves, solitons, chaos. Berlin, Germany: Springer Science & Business Media.
- 20. Chetverikov AP, Sergeev KS. 2018 Dissipative solitons and metastable states in a chain of active particles. *Int. J. Bifurcation Chaos* 28, 1830027. (doi:10.1142/S0218127418300276)
- 21. Hirota R, Suzuki K. 1973 Theoretical and experimental studies of lattice solitons in nonlinear lumped networks. *Proc. IEEE* **61**, 1483–1491. (doi:10.1109/PROC.1973.9297)
- 22. Singer AC, Oppenheim AV. 1999 Circuit implementations of soliton systems. *Int. J. Bifurcation Chaos* **9**, 571–590. (doi:10.1142/S0218127499000419)
- 23. Makarov V, Del Rio E, Ebeling W, Velarde M. 2001 Dissipative Toda-Rayleigh lattice and its oscillatory modes. *Phys. Rev. E* **64**, 036601. (doi:10.1103/PhysRevE.64.036601)
- 24. Kotwal T, Ronellenfitsch H, Moseley F, Dunkel J. 2019 Active topolectrical circuits. (http://arxiv.org/abs/1903.10130)
- 25. Thomson SJ, Couchman MMP, Bush JWM. In press. Collective vibrations of confined levitating droplets. *Phys. Rev. Fluids*.
- 26. Couder Y, Protière S, Fort E, Boudaoud A. 2005 Dynamical phenomena: walking and orbiting droplets. *Nature* **437**, 208. (doi:10.1038/437208a)
- 27. Bush JWM. 2015 Pilot-wave hydrodynamics. *Annu. Rev. Fluid Mech.* 47, 269–292. (doi:10.1146/annurev-fluid-010814-014506)
- 28. Bechinger C, Di Leonardo R, Löwen H, Reichhardt C, Volpe G, Volpe G. 2016 Active particles in complex and crowded environments. *Rev. Mod. Phys.* 88, 045006. (doi:10.1103/RevModPhys.88.045006)
- 29. Löwen H. 2020 Inertial effects of self-propelled particles: from active Brownian to active Langevin motion. *J. Chem. Phys.* **152**, 040901. (doi:10.1063/1.5134455)
- 30. Protière S, Boudaoud A, Couder Y. 2006 Particle–wave association on a fluid interface. *J. Fluid Mech.* **554**, 85–108. (doi:10.1017/S0022112006009190)
- 31. Kim S, Park SH, Ryu C. 1997 Multistability in coupled oscillator systems with time delay. *Phys. Rev. Lett.* **79**, 2911. (doi:10.1103/PhysRevLett.79.2911)
- 32. Kuramoto Y, Battogtokh D. 2002 Coexistence of coherence and incoherence in nonlocally coupled phase oscillators. (http://arxiv.org/abs/cond-mat/0210694)
- 33. Abrams DM, Strogatz SH. 2004 Chimera states for coupled oscillators. *Phys. Rev. Lett.* 93, 174102. (doi:10.1103/PhysRevLett.93.174102)
- 34. Sethia GC, Sen A, Atay FM. 2008 Clustered chimera states in delay-coupled oscillator systems. *Phys. Rev. Lett.* **100**, 144102. (doi:10.1103/PhysRevLett.100.144102)
- 35. Martens EA, Thutupalli S, Fourrière A, Hallatschek O. 2013 Chimera states in mechanical oscillator networks. *Proc. Natl Acad. Sci. USA* 110, 10563–10567. (doi:10.1073/pnas. 1302880110)

- 36. Wojewoda J, Czolczynski K, Maistrenko Y, Kapitaniak T. 2016 The smallest chimera state for coupled pendula. *Sci. Rep.* **6**, 1–5. (doi:10.1038/s41598-016-0001-8)
- 37. Couchman MMP, Bush JWM. In press. Free rings of bouncing droplets: dynamics and stability. *J. Fluid Mech.*
- 38. Oza AU, Rosales RR, Bush JWM. 2013 A trajectory equation for walking droplets: hydrodynamic pilot-wave theory. *J. Fluid Mech.* **737**, 552–570. (doi:10.1017/jfm.2013.581)
- 39. Galeano-Rios CA, Couchman MMP, Caldairou P, Bush JWM. 2018 Ratcheting droplet pairs. *Chaos* 28, 096112. (doi:10.1063/1.5032116)
- 40. Moláček J, Bush JWM. 2013 Drops walking on a vibrating bath: towards a hydrodynamic pilot-wave theory. *J. Fluid Mech.* **727**, 612–647. (doi:10.1017/jfm.2013.280)
- 41. Fort E, Eddi A, Boudaoud A, Moukhtar J, Couder Y. 2010 Path-memory induced quantization of classical orbits. *Proc. Natl Acad. Sci. USA* **107**, 17515–17520. (doi:10.1073/pnas.1007386107)
- 42. Eddi A, Sultan E, Moukhtar J, Fort E, Rossi M, Couder Y. 2011 Information stored in Faraday waves: the origin of a path memory. *J. Fluid Mech.* 674, 433–463. (doi:10.1017/S0022112011000176)
- 43. Couchman MMP, Turton SE, Bush JWM. 2019 Bouncing phase variations in pilot-wave hydrodynamics and the stability of droplet pairs. *J. Fluid Mech.* **871**, 212–243. (doi:10.1017/jfm.2019.293)
- 44. Durey M, Milewski PA, Wang Z. 2020 Faraday pilot-wave dynamics in a circular corral. *J. Fluid Mech.* **891**, A3. (doi:10.1017/jfm.2020.140)
- 45. Oza AU, Siéfert E, Harris DM, Moláček J, Bush JWM. 2017 Orbiting pairs of walking droplets: dynamics and stability. *Phys. Rev. Fluids* **2**, 053601. (doi:10.1103/PhysRevFluids.2.053601)
- 46. Milewski PA, Galeano-Rios CA, Nachbin A, Bush JWM. 2015 Faraday pilot-wave dynamics: modelling and computation. *J. Fluid Mech.* 778, 361–388. (doi:10.1017/jfm.2015.386)
- 47. Durey M, Milewski PA. 2017 Faraday wave–droplet dynamics: discrete-time analysis. *J. Fluid Mech.* **821**, 296–329. (doi:10.1017/jfm.2017.235)
- 48. Turton SE, Couchman MMP, Bush JWM. 2018 A review of the theoretical modeling of walking droplets: toward a generalized pilot-wave framework. *Chaos* 28, 096111. (doi:10.1063/1.5032221)
- 49. Tadrist L, Shim JB, Gilet T, Schlagheck P. 2018 Faraday instability and subthreshold Faraday waves: surface waves emitted by walkers. *J. Fluid Mech.* **848**, 906–945. (doi:10.1017/jfm.2018.358)
- 50. Protière S, Couder Y, Fort E, Boudaoud A. 2005 The self-organization of capillary wave sources. J. Phys.: Condens. Matter 17, S3529. (doi:10.1088/0953-8984/17/45/044)
- 51. Lieber SI, Hendershott MC, Pattanaporkratana A, Maclennan JE. 2007 Self-organization of bouncing oil drops: two-dimensional lattices and spinning clusters. *Phys. Rev. E* **75**, 056308. (doi:10.1103/PhysRevE.75.056308)
- 52. Eddi A, Decelle A, Fort E, Couder Y. 2009 Archimedean lattices in the bound states of wave interacting particles. *Europhys. Lett.* **87**, 56002. (doi:10.1209/0295-5075/87/56002)
- 53. Eddi A, Boudaoud A, Couder Y. 2011 Oscillating instability in bouncing droplet crystals. *Europhys. Lett.* **94**, 20004. (doi:10.1209/0295-5075/94/20004)
- 54. Stokes GG. 1880 On the theory of oscillatory waves. *Transactions of the Cambridge Philosophical Society*.
- 55. Kevorkian JK, Cole JD. 2012 *Multiple scale and singular perturbation methods*, vol. 114. Berlin, Germany: Springer Science & Business Media.
- 56. Strogatz SH. 2018 Nonlinear dynamics and chaos: with applications to physics, biology, chemistry, and engineering. Boca Raton, FL: CRC Press.
- 57. Thomson SJ, Ďurey M, Rosales RR. A discrete Ginzburg-Landau equation for an active lattice In preparation.
- 58. Flynn MR, Kasimov AR, Nave JC, Rosales RR, Seibold B. 2009 Self-sustained nonlinear waves in traffic flow. *Phys. Rev. E* **79**, 056113. (doi:10.1103/PhysRevE.79.056113)
- 59. Hagerstrom AM, Murphy TE, Roy R, Hövel P, Omelchenko I, Schöll E. 2012 Experimental observation of chimeras in coupled-map lattices. *Nat. Phys.* **8**, 658–661. (doi:10.1038/nphys2372)
- 60. Tinsley MR, Nkomo S, Showalter K. 2012 Chimera and phase-cluster states in populations of coupled chemical oscillators. *Nat. Phys.* 8, 662–665. (doi:10.1038/nphys2371)
- 61. Totz JF, Rode J, Tinsley MR, Showalter K, Engel H. 2018 Spiral wave chimera states in large populations of coupled chemical oscillators. *Nat. Phys.* **14**, 282–285.

(doi:10.1038/s41567-017-0005-8)